

Article

Solution-Based Synthesis of Sulvanite Cu_3TaS_4 and Cu_3TaSe_4 Nanocrystals

Mimi Liu , Cheng-Yu Lai, Chen-Yu Chang and Daniela R. Radu *

Department of Mechanical and Materials Engineering, Florida International University, Miami, FL 33199, USA; mliu@fiu.edu (M.L.); clai@fiu.edu (C.-Y.L.); chechang@fiu.edu (C.-Y.C.)

* Correspondence: dradu@fiu.edu; Tel.: +1-(305)-348-4506

Abstract: Sulvanites have the parent formula Cu_3MCh_4 . The metal M belongs to group 5 and Ch is a chalcogen. The tantalum sulvanites Cu_3TaS_4 and Cu_3TaSe_4 are predicted to have wide band gaps and p-type conductivity and show promise in optoelectronic applications. Their potential as p-type transparent conductors or efficient photocatalysts for visible-light water splitting is a valuable incentive to explore these materials in their nanoscale form, toward bottom-up processing opportunities. Reported herein are the first syntheses of nanosized Cu_3TaS_4 and Cu_3TaSe_4 sulvanites, which preserve the parent cubic crystal structure but show that morphology at the nanoscale is dependent of the reaction conditions. The two solution-based methods for synthesizing the tantalum S and Se sulvanites result in Cu_3TaS_4 or Cu_3TaSe_4 nanocrystals (NCs) with prismatic morphology, or, in the case of Cu_3TaSe_4 , could lead to core-shell spherical nanostructures. The Cu_3TaS_4 NCs and Cu_3TaSe_4 NCs have good absorption in the UV-Vis region, while the Cu_3TaSe_4 core-shell NCs possess broad absorption bands not only in the UV-Vis but also in the near-infrared region. Photoluminescence measurements of Cu_3TaS_4 and Cu_3TaSe_4 reveal optical bandgaps of 2.54 and 2.32 eV, respectively, consistent with the values measured in bulk. Additionally, the current–voltage (I–V) curve of Cu_3TaS_4 NCs proves its electrical conductivity.

Keywords: sulvanite Cu_3TaS_4 NCs; Cu_3TaSe_4 NCs; TaSe_2 nanoflakes; TaS_2 nanoflakes; transparent semiconductors



Citation: Liu, M.; Lai, C.-Y.; Chang, C.-Y.; Radu, D.R. Solution-Based Synthesis of Sulvanite Cu_3TaS_4 and Cu_3TaSe_4 Nanocrystals. *Crystals* **2021**, *11*, 51. <https://doi.org/10.3390/cryst11010051>

Received: 30 December 2020

Accepted: 7 January 2021

Published: 10 January 2021

Publisher's Note: MDPI stays neutral with regard to jurisdictional claims in published maps and institutional affiliations.



Copyright: © 2021 by the authors. Licensee MDPI, Basel, Switzerland. This article is an open access article distributed under the terms and conditions of the Creative Commons Attribution (CC BY) license (<https://creativecommons.org/licenses/by/4.0/>).

1. Introduction

In the last few years, the tantalum members of the sulvanites family Cu_3MCh_4 (M = V, Nb, Ta, Ch = S, Se) have been predicted to act as p-type transparent conductive materials (TCMs).

Defined as optically transparent and electrically conductive materials, TCMs have a wide variety of applications, from front-surface electrodes for solar cells and flat-panel displays, energy-conserving windows, rear-view mirrors with automatic dimming capability, and other optoelectrical devices to gas sensors and biosensors [1–7]. To date, the most common and readily accessible inorganic transparent conducting materials are transparent conducting oxides (TCOs), generally in the form of indium tin oxide (In_2O_3 : Sn, ITO), fluorine-doped tin oxide (SnO_2 : F, FTO), and aluminum-doped zinc oxide (ZnO : Al), all of which have high transparency and simultaneously high n-type conductivity [1,2,8,9].

Contrary to these well-exploited n-type TCOs, the p-type TCO materials have been explored scarcely due to the difficulty in experimental preparation of p-type TCOs with both p-type doping and high hole mobilities, where the primary difficulty finally lies in the contradiction of the fundamental requirements of p-type TCOs [10]. In a standard p-type TCOs, it is desirable to provide high transparency of metal oxides while simultaneously providing high hole mobility. However, the 2p levels of the oxygen atom that dominate the valence band maximum (VBM) of the metal oxides lie far lower than the valence orbitals of the metallic atoms, resulting in the ionicity of metallic oxides, and in turn causing the strong localization of the hole at the valence-band edge, finally leading to a large hole effective

mass and low hole mobility [11]. Although p-type doping of transparent conducting oxides can be accomplished by introducing holes into metal oxide materials by various doping techniques (e.g., ZnO) [12] strong localization of holes at the valence-band edge of the oxide materials and the compensation by low-energy native defects still impede the extensive exploitation of p-type TCOs [10–13]. Recently, magnesium (Mg) doping of the Cr member of the delafossites family, Mg-CuCrO₂ exhibited high p-type conductivity (220 S cm⁻¹) [14–16]. No other member of this family showed similar behavior, to date. Although the delafossites (CuMO₂, M = Al, Ga, In, Cr, Sc) possess wide band gaps, their p-type conductivity is still not comparable to the standard n-type transparent conductive materials with the highest conductivity > 300 S cm⁻¹ [10]. Moreover, small hole mobilities, holes high effective masses, and expensive fabrication of films with uniaxial orientation impede the further exploration of delafossites [17,18].

The sulvanites are chalcogenides, with typical semiconductor behavior. Cu₃TaS₄ exhibits yellow color, p-type conductivity, and wide bandgap of 2.76 eV, while Cu₃TaSe₄ displays light-brown color, p-type conductivity, and a bandgap of 2.36 eV [19–23]. In both compounds, VBM mainly originates from the hybridization of Cu 3d states and S 3p or Se 4p states, whereas conduction band minimum (CBM) is typically composed of the Ta 5d and chalcogen p states [22,24]. When compared to p-type TCOs, heavier chalcogen atom sulfur or selenium possessing higher-lying p orbitals (S 3p, Se 4p) could hybridize with the valence orbitals of Cu atom, therefore reducing the localization of holes at the valence-band edge. This in turn increases the hole mobility [14]. Furthermore, the hole effective mass of Cu₃MCh₄ exhibits a downward trend along the chalcogenides (Ch = S, Se), and the calculated hole effective mass of Cu₃TaS₄ and Cu₃TaSe₄ are 0.944 and 0.831 m_h^{*}, respectively [25]. The desired p-type TC should have high hole mobility, light hole effective mass, and high transparency (wide bandgap) making Cu₃TaS₄ and Cu₃TaSe₄ good p-type TC candidates [6].

Thin film TCs are usually fabricated through expensive vacuum-assisted methods. The desired replacement with solution processing methods would contribute significantly to scalability and costs reduction. Solution processing/printing methods usually require nanoscale precursors. However, there are no reports of nanostructured Cu₃TaS₄ and Cu₃TaSe₄.

To date, almost all reports about Cu₃TaS₄ and Cu₃TaSe₄ have been prepared by either solid-state methods or chemical vapor deposition [20,21,26–28]. Compared with the solid-state syntheses, solution-process requires low reaction temperature and is an effective approach to control the morphology and size of the synthesized materials. Furthermore, the solution process allows tailoring of nanocrystals' solubility in a wide variety of solvents by adjusting the surfactants coated on the nanocrystals, therefore facilitating preparation of stable dispersions for further thin film deposition.

In this work, we prepared Cu₃TaS₄ and Cu₃TaSe₄ NCs using two methods and show that the final particle shape is process-dependent. In one approach a cascade synthesis involved preparation of the binary chalcogenide TaS₂ or TaSe₂ with 2D nanoflake morphology followed by addition of Cu cations to form the Cu₃TaSe₄ or Cu₃TaS₄, respectively. The two processes result in nanoparticles with rectangular prismatic morphology, as showed by transmission electron microscopy (TEM), with the sulfur sulvanite NCs forming in one hour, while the selenide counterpart requiring only 10 min.

In an alternative approach, Cu₃TaS₄ NCs could be also synthesized through a one-pot reaction. The introduction of the sulfur source into the hot Cu-Ta cation precursor solution at 300 °C leads to cubic Cu₃TaS₄. The injection of Cu and Ta precursors in the sulfur solution is not possible due to the fast evaporation of CS₂, used as a sulfur source. However, injection of Cu and Ta precursors into a hot selenium solution at 300 °C is feasible and leads to a surprising core-shell morphology of Cu₃TaSe₄ NCs. The mechanisms of the formation of Cu₃TaS₄ and Cu₃TaSe₄ compounds synthesized through the described methods were investigated by X-Ray powder diffraction (XRD).

The specific absorption spectra of synthesized Cu_3TaS_4 and Cu_3TaSe_4 were obtained by UV-Vis-NIR.

As proof of concept, the electrical conductivity of Cu_3TaS_4 NCs was determined by I-V examination of printed Cu_3TaS_4 thin-films.

2. Materials and Methods

2.1. Materials

All chemicals used in this work were used as received without further purification. Tantalum(V) Chloride (TaCl_5 , 99.99%), copper(II) chloride dihydrate ($\text{CuCl}_2 \cdot 2\text{H}_2\text{O}$, 99.999%), carbon disulfide (CS_2 , $\geq 99\%$), formamide (FA, $\geq 99\%$), oleylamine (OLA, 70%), and 1-octadecene (ODE, 90%) were purchased from Sigma-Aldrich (Saint Louis, MI, USA). Selenium powder (Se, 99.99%) and 1-dodecanethiol (1-DDT, $\geq 98\%$) were ordered from Aldrich. Sodium sulfide (Na_2S , anhydrous) was purchased from Alfa Aesar. Ethanol was purchased from Decon lab. ACS grade chloroform (CHCl_3 , $\geq 99.8\%$) was bought from Fisher Scientific (Waltham, MA, USA). Microscope slides were bought from Globe Scientific Inc. (Mahwah, NJ, USA).

2.2. Characterization

X-ray diffraction was performed with a Siemens Diffractometer D5000 (München, Bavaria, Germany) ($\text{Cu K}\alpha$ radiation, $\lambda = 1.5405 \text{ \AA}$) used to determine the crystal structures of synthesized sulvanites. Raman spectra collected on the Raman Renishaw microscope (West Dundee, IL, USA) with 633 nm laser were used to determine purity of the prepared products. Philips CM200 Transmission electron microscopy (TEM) (Hillsboro, OR, USA) was used to investigate the shape and size of the synthesized TaS_2 , TaSe_2 nanoflakes, Cu_3TaS_4 NCs, and Cu_3TaSe_4 NCs. A JEOL 6330F Scanning Electron Microscope (SEM) (Peabody, MA, USA) equipped with EDS was used at 25.0 kV accelerating voltage to determine the elemental distribution of the synthesized Cu_3TaS_4 NCs and Cu_3TaSe_4 NCs. Photoluminescence (PL) spectra of the synthesized Cu_3TaS_4 NCs and Cu_3TaSe_4 NCs were conducted on PERKIN ELMER LS-55 Luminescence Spectrometer (Waltham, MA, USA). The absorption spectra of the synthesized Cu_3TaS_4 NCs and Cu_3TaSe_4 NCs were collected using Agilent Cary 5000 UV-vis-NIR spectrophotometer (Santa Clara, CA, USA). An automated gold sputter coater (PELCO[®]SC-7) was used to fabricate gold electrodes on glass with 100 nm thickness and 1 cm length. The PINE Research WaveNow Potentiostat (Durham, NC, USA) was used to determine the electrical conductivity behavior of the Cu_3TaS_4 and Cu_3TaSe_4 .

2.3. Preparation of TaS_2 Nanoflakes

TaS_2 nanoflakes were synthesized by a hot-injection method. In a glove box filled with argon gas, 1 mmol TaCl_2 (358.2 mg), 9 mL OLA, and 6 mL ODE were loaded to a 100 mL of two-neck round-bottom flask sealed with a rubber septum, immediately transferred it to a Schlenk line, and then evacuated at 125 °C for 30 min. At the same time, 2 mL of 1-DDT and 3 mL of OLA were added to a 25 mL two-neck flask and stirred at room temperature under vacuum for 30 min. Afterward, the temperature of Ta precursor solution was raised to 300 °C under an argon atmosphere, at which point the S precursor solution was injected dropwise into the Ta precursor. The S precursor solution was prepared by adding 0.5 mL CS_2 to a syringe containing a mixture of 2 mL degassed 1-DDT and 3 mL degassed OLA. The reaction was maintained at 300 °C for 2 h and then quenched by removing the heating source. The resulting product was washed with chloroform (CHCl_3) and ethanol ($\text{C}_2\text{H}_5\text{OH}$) in a 1:3 volume ratio. (V:V, 1:3) three times, followed by drying in a vacuum oven overnight.

2.4. Cascade Synthesis of Cu_3TaS_4 NCs

Herein, the Cu_3TaS_4 NCs were prepared by the incorporation of Cu cations in to formed TaS_2 . In a typical synthesis, a pre-prepared Cu precursor solution was injected into the TaS_2 suspension formed above at 300 °C under an argon atmosphere, and then the

reaction was held at 300 °C for different times. The Cu precursor solution was made via dissolving 1.55 mmol $\text{CuCl}_2 \cdot 2\text{H}_2\text{O}$ (264.3 mg) into 5 mL of OLA. Afterward, the reaction was cooled to room temperature by removing the heating source. The product was washed three times with a mixture of chloroform and ethanol (V:V, 1:3). The collected precipitates were dried overnight in a vacuum oven.

2.5. Hot-Injection Synthesis of Cu_3TaS_4 NCs

In a typical experiment, in a glove box filled with argon, 1.5 mmol TaCl_5 (537.5 mg) were added to a 100 mL two-neck round-bottom flask containing a mixture of OLA (9 mL) and ODE (6 mL). The reaction flask was sealed with a rubber septum, transferred to a Schlenk line system, and evacuated at 125 °C for 30 min, whereby a colorless, transparent solution was formed. Simultaneously, 3 mmol $\text{CuCl}_2 \cdot 2\text{H}_2\text{O}$ (511.5 mg) was dissolved in 5 mL OLA in a 25 mL flask and degassed at 100 °C for 30 min. 2 mL of 1-DDT and 3 mL of OLA in a 25 mL two-neck flask were degassed at room temperature for 30 min. After degassing, each of the three flasks was filled with argon. The formed Cu precursor solution was injected into the Ta precursor at 125 °C, and the reaction mixture was heated to 300 °C, where the formation of a brown, transparent solution was observed. When the Cu-Ta solution reached the target temperature, the sulfur source CS_2 (0.5 mL) was added to a syringe containing a mixture of 2 mL degassed 1-DDT and 3 mL degassed OLA, and then injected dropwise into the brown Cu-Ta solution which immediately turned black. The final reaction mixture was held at 300 °C for 1 h, followed by cooling down to room temperature through removing the heating mantle. The resulting yellow product was purified with chloroform and ethanol (V:V, 1:3) three times. The obtained precipitates were dried in a vacuum oven overnight for further analysis.

2.6. Preparation of TaSe_2 Nanoflakes

In a glove box, TaCl_5 (1 mmol, 358.2 mg), Se (2 mmol, 158 mg), 6 mL of ODE, and 9 mL of OLA were loaded to a 100 mL two-neck round-bottom flask under argon atmosphere. This reaction flask was sealed with a rubber septum and then connected to a Schlenk line, followed by stirring for 15 min under vacuum at room temperature. Afterward, the reaction was heated to 305 °C in 30 min and then maintained at 305 °C for 1 h. Finally, cooled down the reaction to room temperature by removing the heating source. The precipitates were purified with chloroform and ethanol (V:V, 1:3) for three times.

2.7. Cascade Synthesis of Cu_3TaSe_4 NCs

Similar to the cascade synthesis of Cu_3TaS_4 NCs, the Cu_3TaSe_4 NCs were prepared using the pre-prepared TaSe_2 nanoflakes as the starting material. In a typical synthesis, the TaSe_2 nanoflakes were grown at 305 °C for 1 h, followed by injecting Cu precursor solution into the TaSe_2 suspension. The reaction was further maintained at 305 °C for 1 h. The Cu precursor solution was prepared by dissolving $\text{CuCl}_2 \cdot 2\text{H}_2\text{O}$ (1.45 mmol, 248 mg) into 5 mL OLA. Afterward, the reaction was cooled down by removing the heating plate. The precipitates were purified with a mixture of chloroform (CHCl_3) and ethanol ($\text{C}_2\text{H}_5\text{OH}$) in a 1:3 volume ratio, three times. The collected product was dried in a vacuum oven overnight for further characterization.

2.8. Hot-Injection Synthesis of Cu_3TaSe_4 NCs

In the hot-injection synthesis of Cu_3TaSe_4 NCs, the elemental Se powder was used as the Se source while TaCl_5 and $\text{CuCl}_2 \cdot 2\text{H}_2\text{O}$ served as Ta and Cu source, respectively. In a 100 mL two-neck round-bottom flask, 158 mg Se powder (2 mmol), 9 mL OLA, and 6 mL ODE were loaded to prepare the Se precursor. The Ta precursor was prepared in a 25 mL two-neck round-bottom flask by dissolving 1 mmol TaCl_5 (358.2 mg) into a mixture of 3 mL OLA and 2 mL ODE under argon atmosphere. Meanwhile, 1 mmol $\text{CuCl}_2 \cdot 2\text{H}_2\text{O}$ (170.5 mg) was added to a 25 mL two-neck round-bottom flask containing 5 mL OLA to make the Cu precursor solution. Each of the three precursors was degassed at 120 °C for

30 min and then flushed with argon. Next, the Cu precursor solution was injected into the Ta precursor and then maintained at 120 °C to form a brown Cu-Ta solution. In parallel, the Se precursor was heated to 300 °C, and the Cu-Ta solution was injected immediately into the Se solution. An immediate black color change was observed (within one second). The reaction mixture was held at 300 °C for 1 h. Afterward, the reaction was quenched by removing the heating source. The product was washed with a mixture of chloroform and ethanol (V:V, 1:3) three times, collected, and dried in a vacuum oven overnight.

2.9. Fabrication of Cu_3TaS_4 NCs and Cu_3TaSe_4 Inks

Cu_3TaS_4 inks were prepared by dispersing 30 mg of Cu_3TaS_4 NCs into 1 mL of ethanol using probe ultrasonication for 20 min. Cu_3TaSe_4 inks were prepared by the same dispersion method. Each ink was prepared from NCs that were subjected first to ligand exchange, toward removing residual OLA remaining on the NCs surface from synthesis and replace them with S^{2-} . The ligand exchange of Cu_3TaS_4 NCs and Cu_3TaSe_4 NCs followed a previously reported process for Cu_3VSe_4 NCs [29]. In a typical experiment, Cu_3TaS_4 NCs were suspended in chloroform (8 mg/mL). Then, 10 mL of this suspension was transferred to a 50 mL tube containing 10 mL of Na_2S solution in formamide (0.2 M). Next, the mixture was vigorously shaken for 1 min and further allowed to rest until ligand exchange completion, when Cu_3TaS_4 NCs were fully transferred from the chloroform phase (lower) to the formamide phase (upper). Afterward, the clear chloroform phase was removed, and 5 mL distilled water and 20 mL of ethanol was added to the aqueous phase to precipitate the Cu_3TaS_4 NCs. The precipitate was purified by washing it twice with a mixture of ethanol and distilled water (ethanol:water = 4:1) followed by washing with a mixture of toluene and ethanol (toluene:ethanol = 1:3). The resulting product was collected and dried in a vacuum oven overnight. The same process was followed for Cu_3TaSe_4 NCs ligand exchange.

2.10. Fabrication of Cu_3TaS_4 NCs and Cu_3TaSe_4 NCs Thin Films and Devices

To evaluate the electrical conductivity of the Cu_3TaS_4 NCs and Cu_3TaSe_4 NCs, thin films were fabricated with each of the NCs on glass, as follows. First, the glass slides were washed with distilled water, acetone, and methanol in sequence for 5 min each solvent, using an ultrasonic bath. Then, gold was coated on a clean glass substrate by using an Au sputter coater to fabricate two gold electrodes with a thickness of 100 nm and a width of 1 cm, leaving a separation of 1 cm between two Au electrodes. Afterward, an amount of 10 μL of Cu_3TaS_4 or Cu_3TaSe_4 inks (30 mg/mL) was coated to the inter-electrode gap by bar-coating (as depicted in Figure 7a). The thin film was dried in air at 100 °C for 1 min using a hot plate. The coating and drying process was repeated twice to manufacture the Cu_3TaS_4 NCs and Cu_3TaSe_4 NCs-based devices.

3. Results and Discussion

3.1. TaS_2 Nanoflakes Characterization

The crystal structure of the synthesized TaS_2 was identified from the XRD pattern shown in Figure 1a, exhibiting two characteristic peaks at 30.6 and 54.6 degrees, which could be indexed to the hexagonal TaS_2 phase (PDF# 04-003-1715) with a space group of $\bar{P}3m1$. It is worth noting that the peak intensity ratio of the synthesized TaS_2 is not the same as the indexed pattern which could be attributed to the preferential growth of the two-dimensional (2D) nanostructures in specific crystallographic directions with a high aspect ratio. Figure 1b illustrates the crystal structure of TaS_2 . A low-magnification TEM image of the synthesized TaS_2 is showed in Figure 1c. Notably, the TaS_2 exhibit thin nanoflake morphological features, with nanosheet size ~150nm in diameter. A stacking of the nanoflakes is observed.

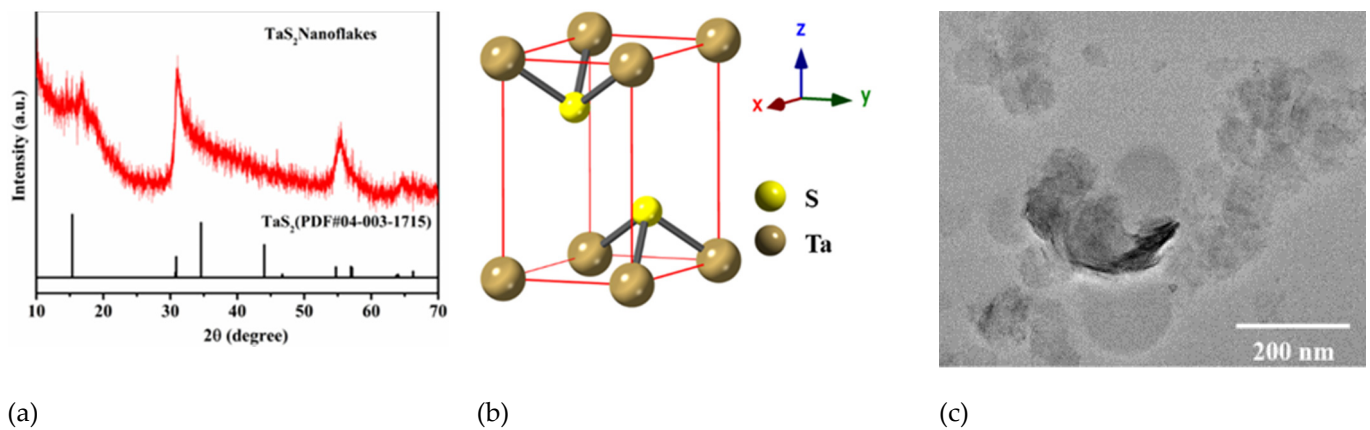


Figure 1. Characterization of the synthesized TaS₂ nanoflakes. (a) XRD pattern. (b) Crystal structure. (c) TEM image.

3.2. Cu₃TaS₄ NCs

3.2.1. Characterization of Cu₃TaS₄ NCs

XRD patterns of the products prepared using either the cascade method or the hot-injection method (Figure 2a) shows a single cubic Cu₃TaS₄ phase with a space group of *P43m*, however, the product colors are different: Cu₃TaS₄ NCs (inset) synthesized using hot-injection is yellow, while the Cu₃TaS₄ NCs synthesized using the cascade method, displays a mustard-green color. Through investigating Cu₃TaS₄ NCs prepared with different amounts of Cu incorporation, we speculated that the variety in the color of the products should be caused by different amounts of Cu insertion. In the hot-injection synthesis of Cu₃TaS₄ NCs, when we added the Cu, Ta, and S precursors with stoichiometric ratio, the obtained product showed dark green and a mixture of Cu₂S and Cu₃TaS₄ phases, as shown in supporting information (Supplementary Materials Figure S1). A comparison of Raman spectrum of the Cu₃TaS₄ NCs synthesized using cascade method and hot-injection in Figure 2b shows two identical dominant Raman scattering peaks at around 264.1 cm⁻¹ and 413 cm⁻¹, which correspond to the A₁ mode of Cu-S bond and A₁ vibration mode of Ta-S bond of Cu₃TaS₄, respectively, in good agreement with the previous reports [30]. Our recent report showed that a cascade synthesis of Cu₃VSe₄ from VSe₂ nanosheets leads to a preservation of nanosheet morphology [31]. In this light, it was expected that Cu₃TaS₄ formed using the same method will facilitate the preservation of nanosheets. However, Cu₃TaS₄ was formed in cubic shape with an average size of around 20 nm (Figure 2c), without maintaining the 2D morphology of the TaS₂ nanoflakes template. Earlier reports show such example of the transformation from nanosheets to nanodisks upon adding the third cation, in the case of CuInS₂ [32]. Ultrathin γ-In₂S₃ nanosheets were turned into CuInS₂ nanodisks when incorporating the Cu⁺ ions. In this case it was hypothesized that the reason for the formation of CuInS₂ nanodisks from γ-In₂S₃ nanosheets during colloidal synthesis is that the incorporation of Cu⁺ caused additional strain, which will lead the folded nanosheets to tear into nanodisks [32]. Thus, we posit that the insertion of Cu cations during the preparation of Cu₃TaS₄ NCs by cascade method caused additional stress which resulted in tearing of the folded TaS₂ nanoflakes into cubic nanocrystals in the solution process. Similarly, the TEM image (Figure 2c) of the Cu₃TaS₄ NCs prepared by hot-injection presents cubic shape with a smaller particle size of ~15 nm. The SEM-EDS elemental mapping of the synthesized Cu₃TaS₄ using the cascade method (Figure 3) shows a homogeneous distribution of Cu, Ta, and S elements.

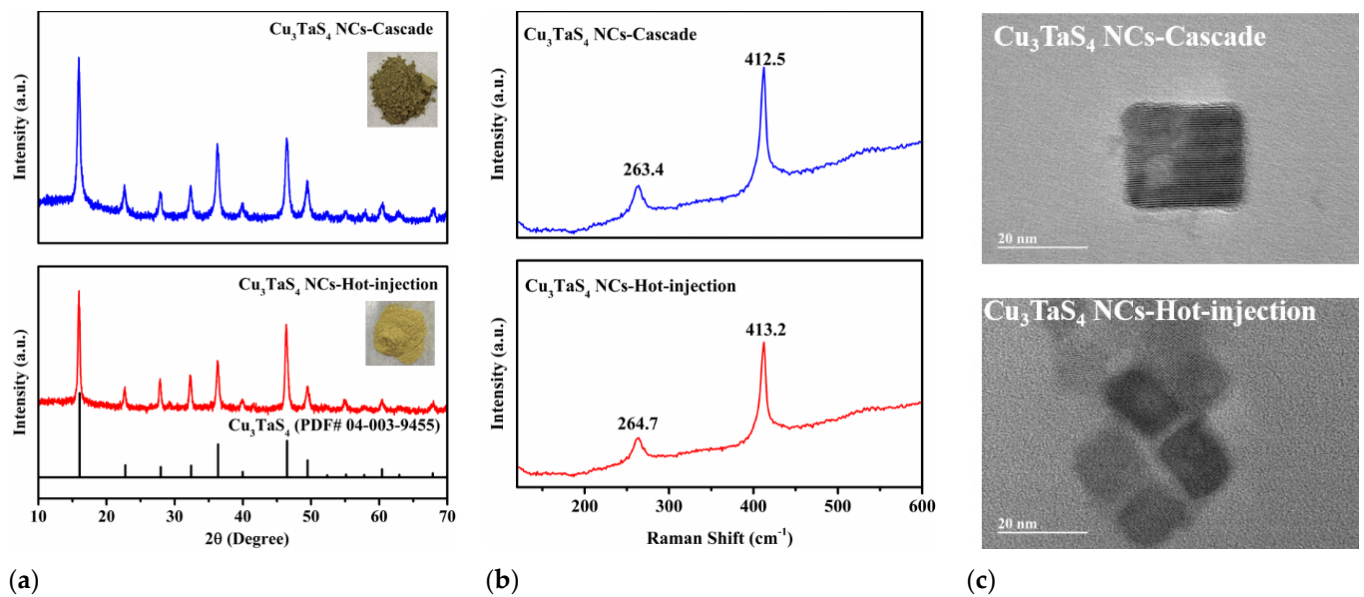


Figure 2. Characterization of Cu_3TaS_4 NCs prepared by cascade and hot-injection method. (a) XRD pattern. (b) Raman spectra. (c) TEM images.

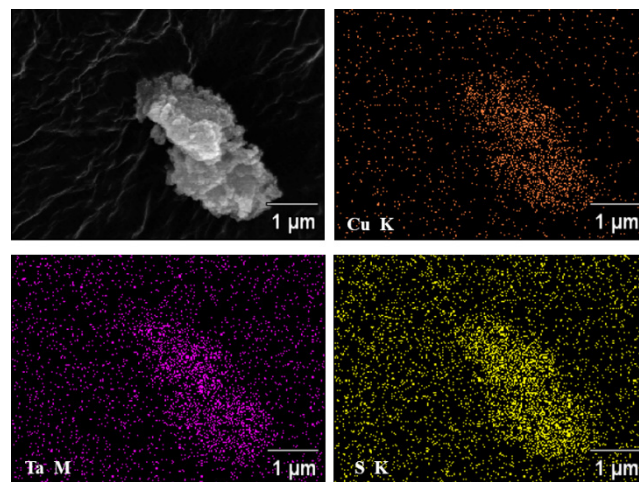


Figure 3. SEM-EDS mapping of Cu_3TaS_4 NCs by cascade method.

3.2.2. Mechanism of Cu_3TaS_4 NCs Cascade Synthesis

To get an insight into the mechanism of Cu_3TaS_4 NCs formation through cascade synthesis, a series of experiments with different reaction times were carried out, and the XRD patterns of the obtained products (Figure 4) were used to investigate the phase transformations during the process. Upon the addition of Cu cations to the formed TaS_2 nanoflakes, a rapid phase transition from hexagonal TaS_2 to cubic Cu_3TaS_4 happened, which was observed to occur within 1 min. Additionally, when extending the reaction time to 1 h, neither secondary phase nor other crystalline impurities were detected, however, the color of the products gradually changed from black to yellow, and the crystallinity and yield of products were enhanced. The color changes of the product with the reaction time are detailed in the Supplementary Figure S2a. The phase transformation identified by XRD patterns proved that there was a major rearrangement of atoms in the TaS_2 nanoflakes when inserting Cu cations. Herein, the ultrathin template of TaS_2 nanoflakes was considered to be the key to the rapid synthesis of Cu_3TaS_4 nanocrystals, since the large surface area and high aspect ratio of the 2D nanostructures provide more reaction sites, thereby promoting

the migration of Cu cations and rearrangement of atoms, which finally accelerates the formation of Cu_3TaS_4 nanocrystals.

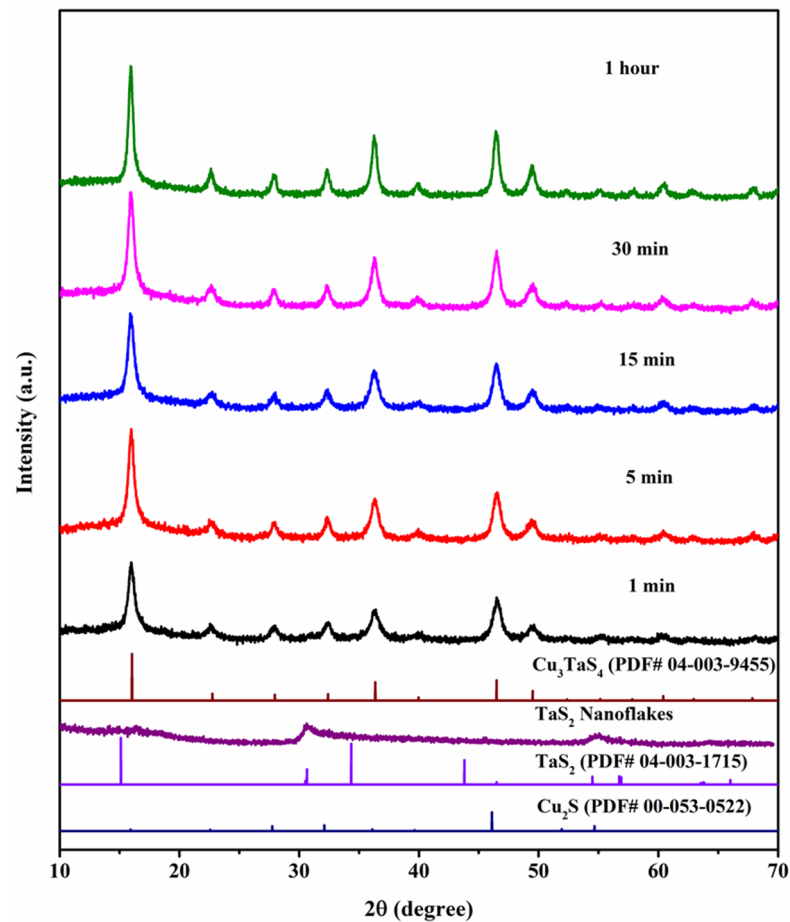


Figure 4. Mechanism for cascade synthesis of Cu_3TaS_4 NCs.

3.2.3. Mechanism for Hot-Injection of Cu_3TaS_4 NCs

Briefly, the hot-injection method involves the injection of a cold reagent into hot precursors to trigger rapid nucleation which is followed by a crystal growth step. Figure 5 compares the XRD patterns of the Cu_3TaS_4 NCs products obtained at different reaction times after adding the sulfur source. The color changes of the products are shown in the Supporting Information (Supplementary Materials Figure S2b). Given that the primary XRD peak positions of the Cu_2S (PDF# 00-053-0522) are close to those of Cu_3TaS_4 (PDF# 04-003-9455), we considered the distinguished peak at 49.5° 2θ (marked by the red dotted line) to be the indicative of the presence of the Cu_3TaS_4 . As shown in Figure 5, 1 min after adding the S source into the Cu-Ta precursors, the XRD of the product showed a Cu_2S phase. As noted above, after 30 min, a characteristic peak at 49.5° 2θ appeared in the XRD pattern, indicating the formation of the cubic Cu_3TaS_4 phase. As the reaction progressed, the XRD peaks intensity of Cu_3TaS_4 gradually increased; at 1 h the intensity of peak at 16.04° grew relatively higher than that of 46.5° , where the peak intensity ratio of 16.04° to 46.5° is close to the indexed pattern, indicating the formation of pure phase of Cu_3TaS_4 . Thus, in the hot-injection synthesis of Cu_3TaS_4 NCs, the swift addition of the sulfur precursor into the Cu-Ta metal precursor at 300°C triggered the rapid nucleation of Cu_2S seeds, and then the formed Cu_2S seeds subsequently reacted with Ta cations to form the Cu_3TaS_4 nanocrystals. Compared with the cascade synthesis of Cu_3TaS_4 NCs that uses TaS_2 nanoflakes as the starting templates, the hot injection method which employs the formed Cu_2S as the starting seeds took a longer time to form Cu_3TaS_4 NCs. We attribute this to the larger radius of Ta cation.

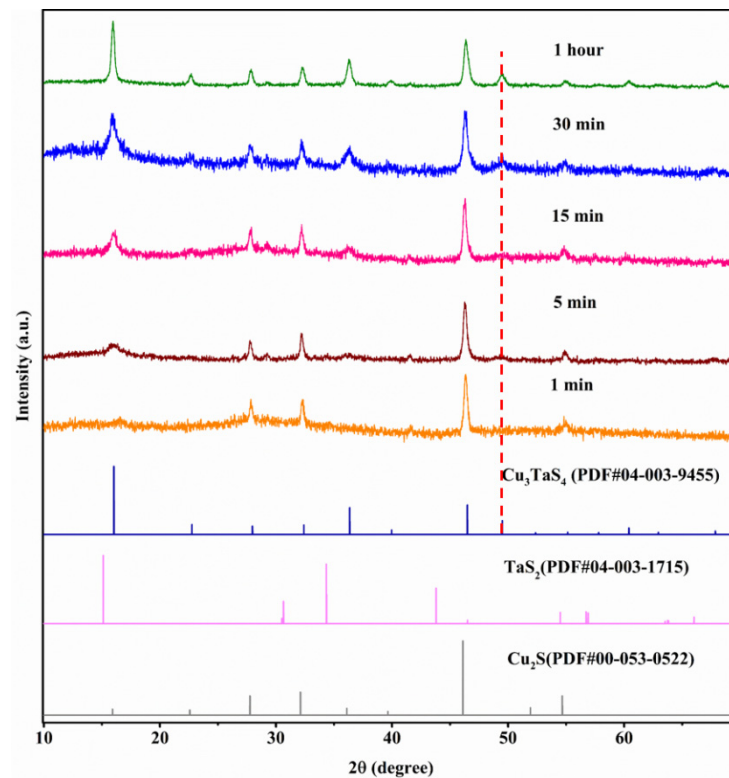


Figure 5. Mechanism for hot-injection synthesis of Cu_3TaS_4 NCs.

3.2.4. Optoelectrical and Conductive Properties of Cu_3TaS_4 NCs

Figure 6a depicts the optical absorption spectrum of the synthesized Cu_3TaS_4 NCs in the ultraviolet, visible, and near-infrared regions, which shows three absorbance bands at around 267.1, 300.8 and 352.6 nm. Figure 6b shows the photoluminescence (PL) spectrum of the synthesized Cu_3TaS_4 NCs in ethanol, when using 360 nm as the excitation wavelength, the characteristic emission peaks occurred at 486.3 and 531.4 nm, corresponding to 2.54 eV and 2.33 eV, respectively. The green emission at 531.4 nm indicated a mid-band-gap charge trap caused by Cu vacancies near the valence band maximum, in good agreement with a previous report by Hersh [21], where green photoemission at 548 nm was present for the Cu_3TaS_4 single crystal.

To evaluate the electrical conductivity of the Cu_3TaS_4 NCs, a Cu_3TaS_4 NCs-based device with a configuration of Au/ Cu_3TaS_4 NCs-glass/Au was subjected to an I - V measurement. The schematic of the device configuration for the I - V measurement is shown in Figure 7a. The I - V curve of the Au/ Cu_3TaS_4 NCs-glass/Au device is shown in Figure 7b blue line, where the current progressively increases along with the voltage bias towards positive, implying the electrons could flow through the Cu_3TaS_4 NCs area. Generally, glass is a good insulator that does not allow the flow of electrons, and its conductivity is negligible as compared to the material of the thin films. Thus, it could be concluded that in the Au/ Cu_3TaS_4 NCs-film/Au device, the electrons flow through the Cu_3TaS_4 NCs thin film rather than the glass substrate. To prove our hypothesis, we prepared a control device configured as Au/Glass/Au, where the two gold electrodes connected only by clean glass. The I - V curves of the control device are shown in Figure 7b red line, where the current is kept at around zero amperes when increasing the voltage, suggesting that no electrons flow through the glass substrate, which further evidence our hypothesis that Cu_3TaS_4 material has electrical conductivity. The obtained I - V plot of the Au/ Cu_3TaS_4 NCs-glass/Au device allowed us to calculate the electrical conductivity of Cu_3TaS_4 NCs. Using the equation $R = V/I$ (R -Resistance in ohms(Ω); V -voltage in volts (V); I -current in amperes(A)), we could calculate the resistance of Cu_3TaS_4 NCs, namely, the slope of the I - V curve, which is

$1.49 \times 10^7 \Omega$. Generally, the electrical conductivity of a thin film (σ) could be determined using the following expression:

$$\sigma = \frac{t}{RA}$$

where R is the film resistance between the two electrodes, t is the thickness of the sample, and A is the surface area of the sample [33–39]. Here, R is $1.49 \times 10^7 \Omega$, t is $2.05 \times 10^{-6} \text{ m}$ (determined from SEM cross-section of the film), and A is 10^{-4} m^2 , thus, the calculated electrical conductivity of Cu_3TaS_4 NCs is $1.38 \times 10^{-9} \text{ S}\cdot\text{m}^{-1}$. Although the calculated electrical conductivity is low, this could be attributed to a poor quality of the thin film and poor connection between Au electrodes and Cu_3TaS_4 NCs thin film. The optoelectronic properties of Cu_3TaS_4 NCs suggests that the materials are a promising candidate for the p-type transparent conductor applications.

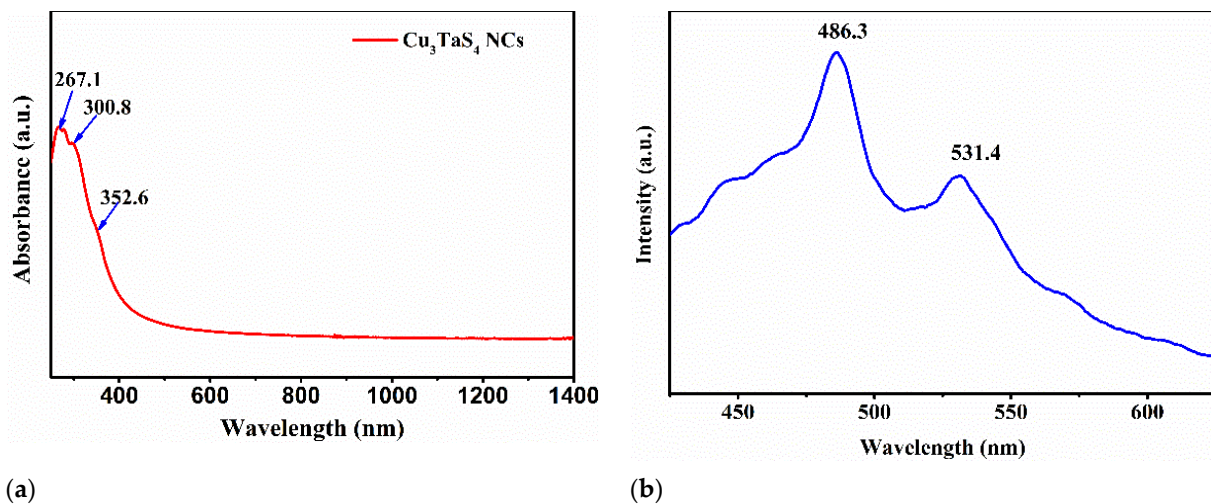


Figure 6. (a) UV-Vis-NIR absorption spectrum. (b) PL spectrum of the synthesized Cu_3TaS_4 NCs in ethanol.

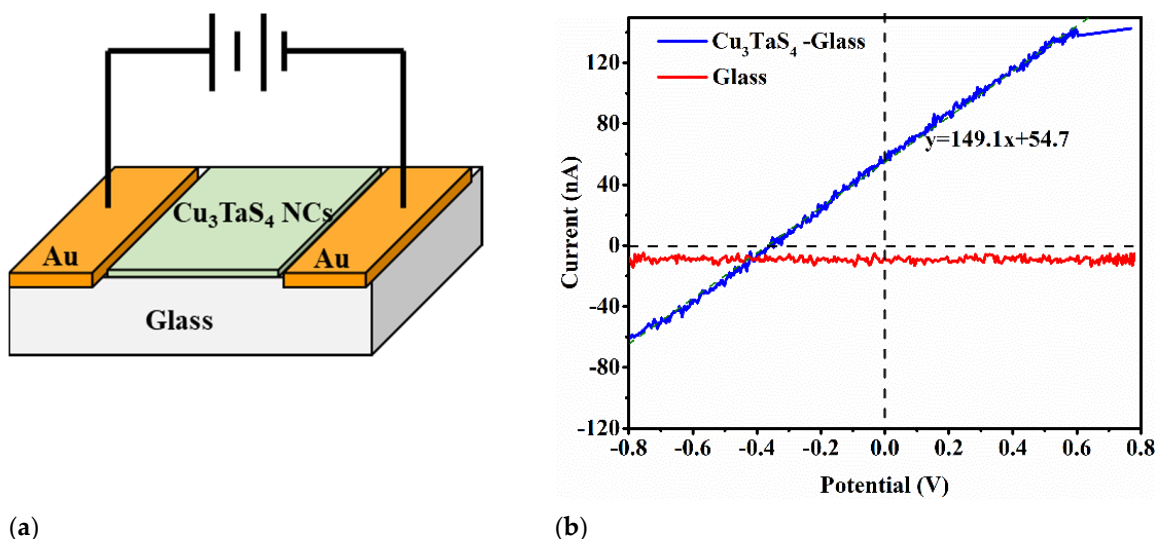


Figure 7. (a) Schematics of the device configuration for the I-V measurement. (b) I-V curve of the Au/ Cu_3TaS_4 NCs-glass/Au device and Au/Glass/Au.

3.3. Characterization of TaSe_2 Nanoflakes

The crystal structure of the synthesized TaSe_2 was analyzed by powder XRD pattern as shown in Figure 8a, which is in good agreement with the patterns reported by Jeong et al. [40], where they assigned the product to the hexagonal TaSe_2 phase (PDF# 04-019-1305) with a space group of $P 6_3/mmc$. The identified crystal structure is shown in Figure 8b.

The TEM image shown in Figure 8c indicates the folded nanoflakes characteristic of the solution synthesized TaSe₂.

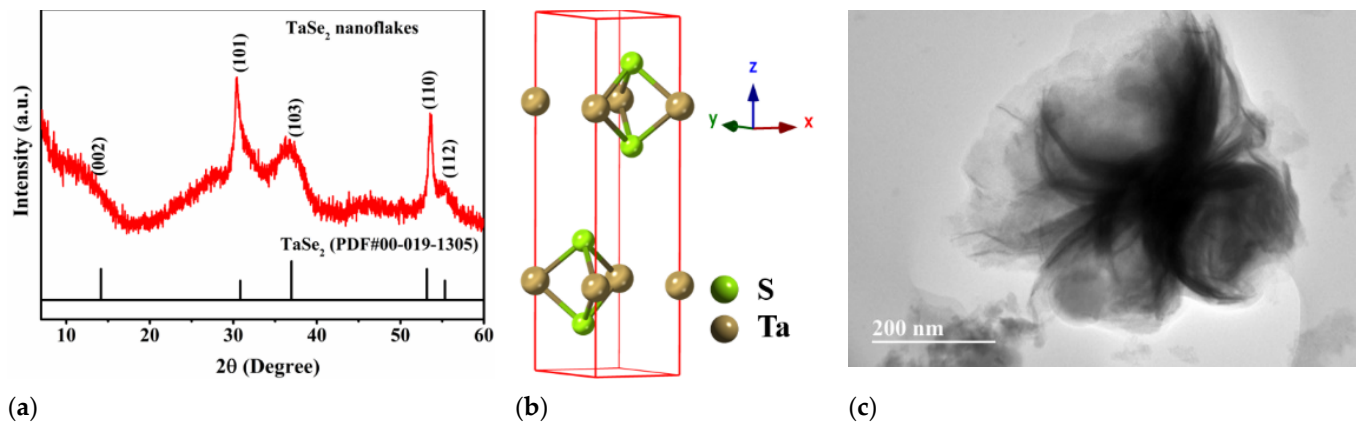


Figure 8. Characterization of synthesized TaSe₂ nanoflakes. (a) XRD pattern. (b) Crystal structure. (c) TEM image.

3.4. Cu₃TaSe₄ NCs

3.4.1. Characterization of Cu₃TaSe₄ NCs

A comparison of XRD pattern for Cu₃TaSe₄ prepared by cascade and hot-injection method is shown in Figure 9a, where the characteristic peaks are the same and match to the cubic Cu₃TaSe₄ with a space group of *P43m* (215). Simultaneously, the Raman scattering peaks of both the cascade synthesized Cu₃TaSe₄ and the Cu₃TaSe₄ prepared by the hot-injection method locate at around 167.4 and 242.8 cm⁻¹, as shown in Figure 9b, which are associated with F₁^b and A₁ mode of Cu₃TaSe₄, respectively [30,41]. In the synthesis of Cu₃TaSe₄, when the Cu, Ta, and Se precursors are added with stoichiometric ratio, the obtained product showed both Cu_{7.16}Se₄ and Cu₃TaSe₄ phases, as shown in supporting information (Figure S3). As noted in the case of cascade synthesized Cu₃TaSe₄ NCs, the synthesized Cu₃TaSe₄ NCs did not maintain the 2D morphology of the TaS₂ nanoflakes because that the incorporation of Cu cations caused additional stress which leads to tearing of the folded TaS₂ nanoflakes into cubic nanocrystals. Similarly, the Cu₃TaSe₄ NCs prepared using the cascade method did not maintain the nanoflake morphology of TaSe₂ template, but instead transformed into cubic shapes with irregular sizes, as shown in Figure 9c.

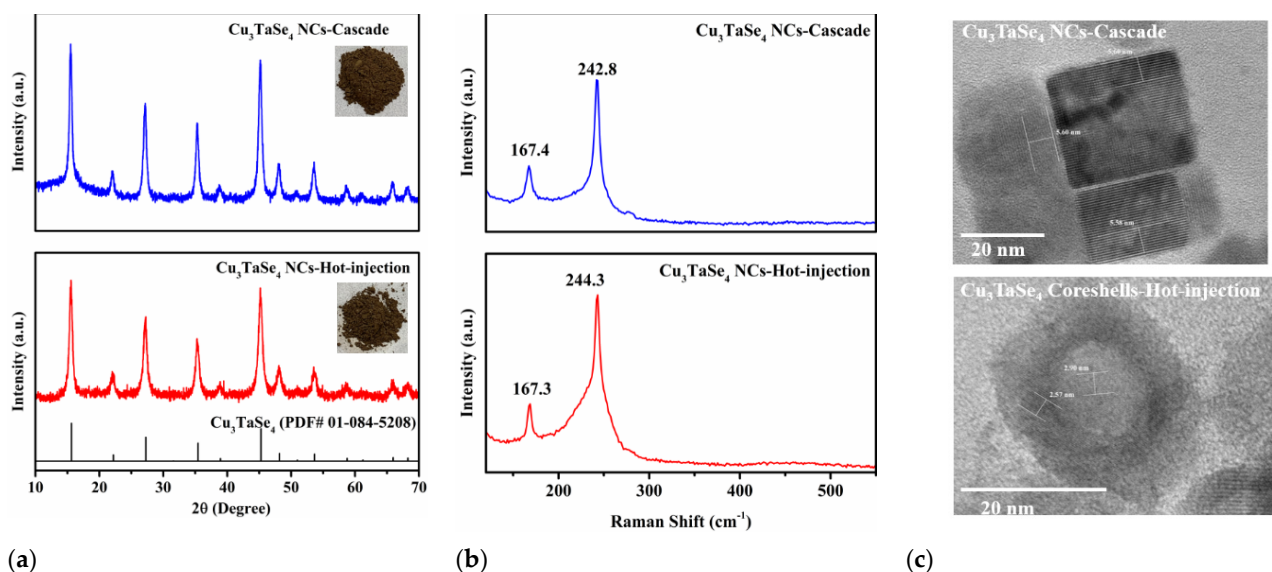


Figure 9. Characterization of Cu₃TaSe₄ prepared by cascade and hot-injection methods. (a) XRD pattern. (b) Raman spectra. (c) TEM images.

In contrast, the TEM image of the synthesized Cu_3TaSe_4 by hot-injection presents a core-shell morphology, where the interplanar spacing of 2.9 \AA in the core region matches to the lattice (200) of cubic Cu_3TaSe_4 , whereas the d-spacing of 2.57 \AA located in the shell field could be attributed to the plane (210). Figure 10 displays the SEM-EDS of the synthesized Cu_3TaSe_4 using cascade synthesis, where Cu, Ta, and Se elements spread homogeneously in the synthesized Cu_3TaSe_4 materials. This suggest that core and shell have the same crystal structure, with different orientation. Further characterization is ongoing.

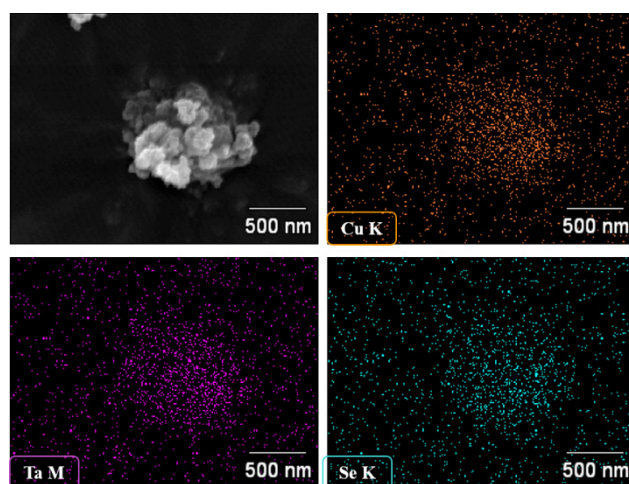


Figure 10. SEM-EDS mapping of Cu_3TaSe_4 NCs synthesized by cascade method.

3.4.2. Mechanism for Cascade Synthesis of Cu_3TaSe_4 NCs

Phase structures of the products obtained at different times after injecting Cu cations were identified from XRD patterns shown in Figure 11. The suspension of formed TaSe_2 nanoflakes in OLA-ODE was used as starting template. The characteristic peaks at 27.04° , 44.89° , and 53.2° 2θ that belong to the cubic $\text{Cu}_{7.16}\text{Se}_4$ were detected 1 min after injecting Cu^{2+} ions into the TaSe_2 suspension. Meanwhile, trace amounts of TaSe_2 residues could also be detected. When the reaction time was extended to 10 min, the characteristic Cu_3TaSe_4 peak at 15.64° started to appear, indicating the formation of Cu_3TaSe_4 . However, it can be noted that the characteristic peaks of $\text{Cu}_{7.16}\text{Se}_4$ at 27.04° , 44.89° , and 53.2° are close to the dominant peaks of Cu_3TaSe_4 at 27.26° , 45.26° , and 53.65° , which makes it difficult to determine the purity of the products. Herein, we take the peak intensity ratio of the peak at 15.64° (100) to 45.26° (220) as the criteria to demonstrate the purity of the synthesized Cu_3TaSe_4 , where the intensity ratio of (100) to (220) for the standard Cu_3TaSe_4 (PDF# 01-084-5208) is 1.08. Thus, when reacting for 10 min after injecting Cu cations, there were three phases in the reaction flask, including $\text{Cu}_{7.16}\text{Se}_4$, TaSe_2 , and Cu_3TaSe_4 . When the reaction time was prolonged to 20 min, the TaSe_2 phase disappeared, and a mixed phase of $\text{Cu}_{7.16}\text{Se}_4$ and Cu_3TaSe_4 were present in the reaction mixture at this stage. When the reaction proceeded for 1 h, the peak intensity ratio of (100) to (220) converted to approximately 1.09, implying that the pure Cu_3TaSe_4 was obtained. These XRD observations suggested that the incorporation of Cu cations triggered the rapid nucleation of $\text{Cu}_{7.16}\text{Se}_4$, and then the formed $\text{Cu}_{7.16}\text{Se}_4$ consumed the folded TaSe_2 nanoflakes to form Cu_3TaSe_4 NCs. The overall color change of the reaction with reaction time is shown in Supporting Information (Figure S4a).

3.4.3. Mechanism for Hot-Injection Formation of Cu_3TaSe_4 NCs

To assess the mechanism of Cu_3TaSe_4 NCs formation using the hot-injection method, we investigated the XRD patterns and color change of products at different reaction times, as shown in Figure 12 and Figure S4b, respectively. Once injecting the Cu-Ta precursor into the hot selenium solution, the first primary phase of $\text{Cu}_{7.16}\text{Se}_4$ was observed in the XRD patterns (Figure 12), indicating that the $\text{Cu}_{7.16}\text{Se}_4$ formed rapidly within 1 min, which

was consistent with the cascade synthesis of Cu_3TaSe_4 NCs. After 5 min, the presence of the XRD peak at 15.64° highlights the formation of the cubic Cu_3TaSe_4 phase. As the reaction proceeded, the peak intensity ratio of the characteristic peak at 15.64° to 45.26 increased gradually, indicating the progressive conversion from $\text{Cu}_{7.16}\text{Se}_4$ to cubic Cu_3TaSe_4 . Therefore, we hypothesize that the formation of Cu_3TaSe_4 NCs could follow the path below.

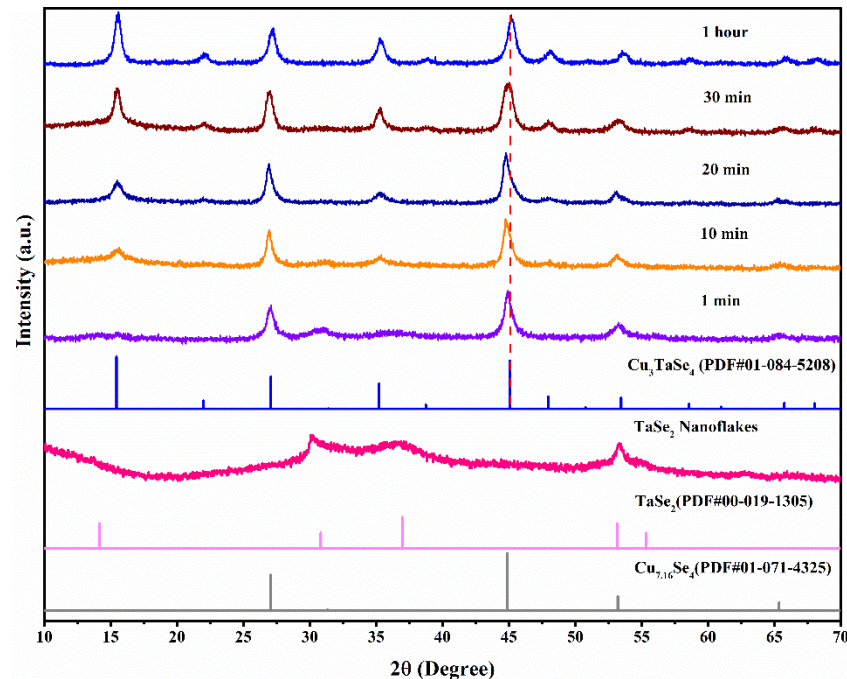
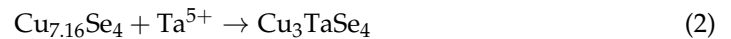
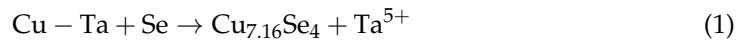


Figure 11. Mechanism for cascade synthesis of Cu_3TaSe_4 NCs.

3.4.4. Optoelectrical and Conductivity Properties of Cu_3TaSe_4 NCs

Optical spectra of synthesized Cu_3TaSe_4 NCs are shown in Figure 13a. The UV-Vis-NIR spectrum of the Cu_3TaSe_4 NCs prepared by the cascade method shows three primary peaks at around 282.6, 339.6, and 393.5 nm, respectively, whereas the spectrum of the Cu_3TaSe_4 core-shells exhibits a broad absorbing band at around 420.3 nm with two small characteristic peaks at 297.8 and 361.5 nm. Compared with the Cu_3TaSe_4 NCs, the UV-Vis-NIR spectrum of Cu_3TaSe_4 core-shells showed an additional absorption band at around 800-1000nm, which is related to the core-shell structured properties of Cu_3TaSe_4 . Photoluminescence spectra of Cu_3TaSe_4 prepared by either the cascade method or hot-injection method (Figure 13b) showed a characteristic peak at around 535 nm, suggesting that the optical bandgap of Cu_3TaSe_4 was 2.32 eV, which is in good agreement with the previous reports [5,21,28,42]. The I-V curve of fabricated Au/ Cu_3TaSe_4 NCs-glass/Au device in Figure S5 shows a weak resistance. The electrical conductivity of Au/ Cu_3TaSe_4 NCs-glass/Au device is very low compared to that of Cu_3TaSe_4 NCs based device. Theoretically, the conductivity of semiconductor is proportional to the product of the mobility and the density of carriers. Herein, as p-type semiconductor, the majority carrier in Cu_3TaSe_4 and Cu_3TaSe_4 semiconductors is the hole, thereby, their conductivity varies depending on the hole mobility and the density of holes. As described in the introduction, the calculated hole effective mass of Cu_3TaSe_4 and Cu_3TaSe_4 are 0.944 and 0.831 m_h^* , Cu_3TaSe_4 has a lighter hole effective mass and should be more likely to display good p-type mobility. However, the defect concentration and the hole concentration could also affect the conductivity of devices. Speculating about the reason for a less conductivity

of Au/Cu₃TaSe₄ NCs-glass/Au device, we could imagine that the fabricated devices would have a high defect density, which would trap the charge carriers or a low hole density of Cu₃TaSe₄ NCs. Further investigations in future studies are necessary to resolve the reason for the low conductivity, such as improving the thin-film quality.

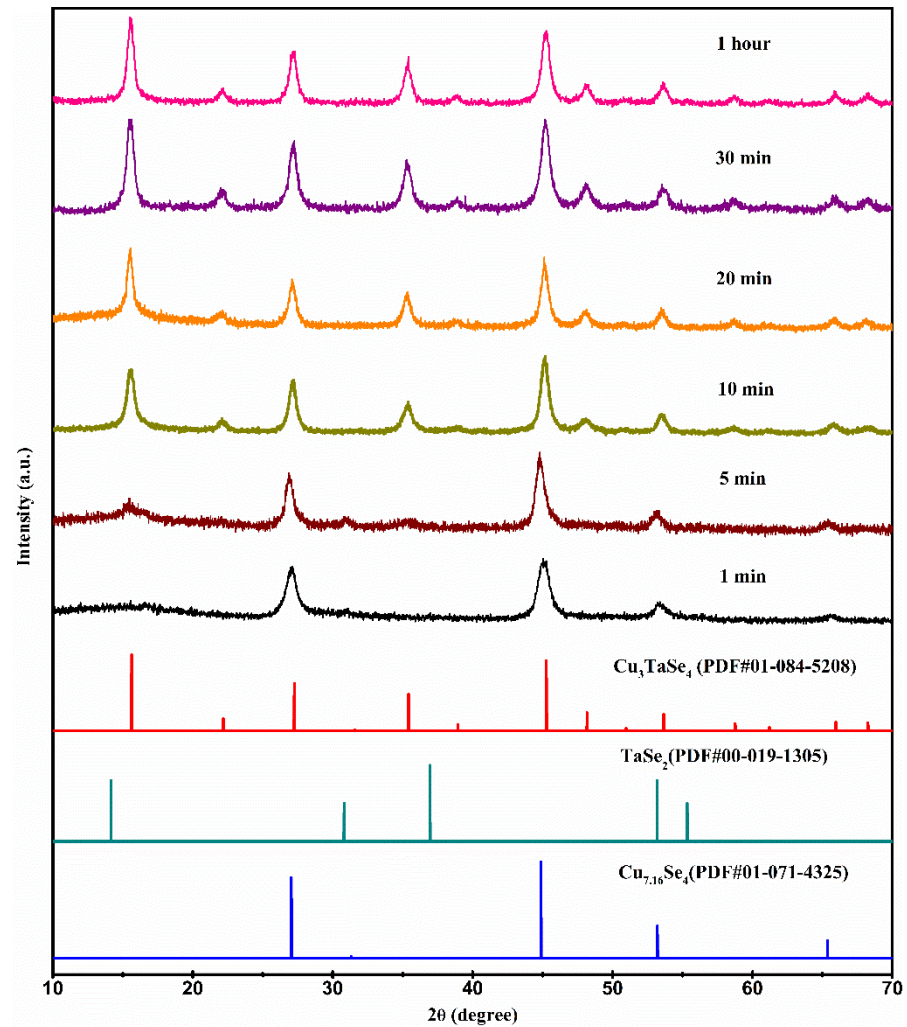


Figure 12. Mechanism for hot-injection of Cu₃TaSe₄ NCs.

Table 1 displays the morphology, size, and performance of the Cu₃TaSe₄ and Cu₃TaSe₄ materials prepared under different experimental conditions. It is known from the table that the reaction temperature for preparing the Cu₃TaSe₄ and Cu₃TaSe₄ materials by the solution-phase method is relatively lower than that of the solid-state method. Thereby, comparing the products prepared by the solid-state method and the solution-process, it is apparent that the solution-phase method is more controllable, facile, and time cost-effective.

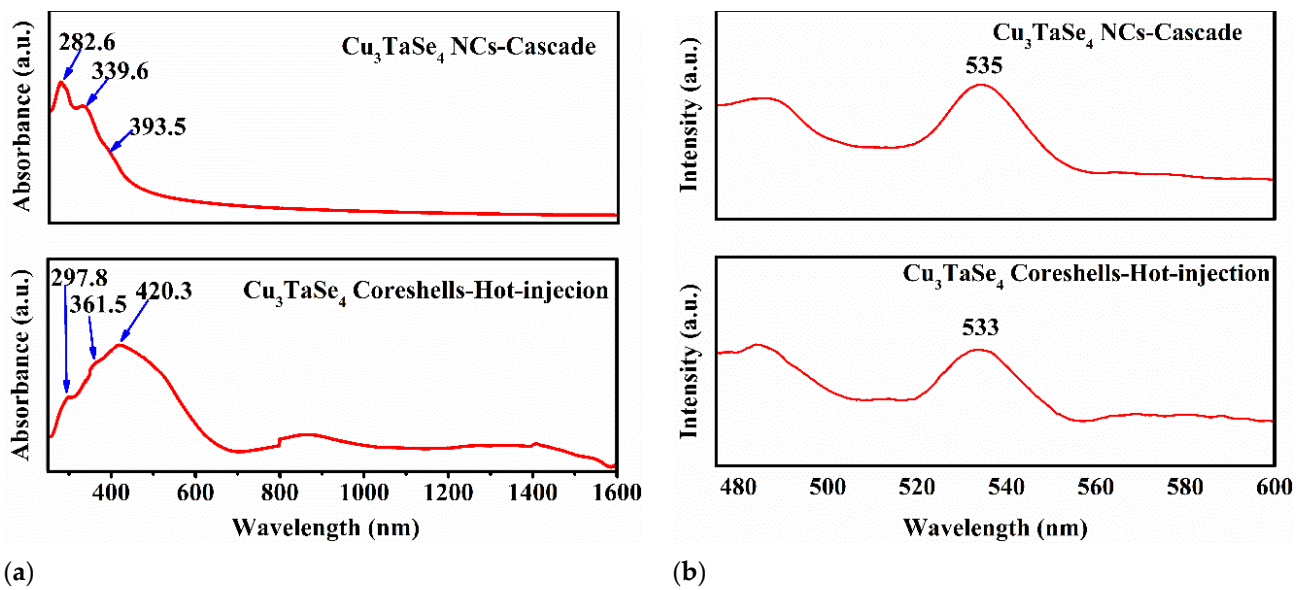


Figure 13. (a) UV-Vis-NIR absorption spectra of Cu_3TaSe_4 NCs and Cu_3TaSe_4 Core-shells. (b) PL spectra of Cu_3TaSe_4 NCs and Cu_3TaSe_4 Core-shells.

Table 1. Experimental conditions and performance of Cu_3TaS_4 and Cu_3TaSe_4 nanomaterials synthesized with different methods.

Compound	Synthesis Method	Formation Condition	Shape and Dimension	Performance	
				Color	Conductivity
Cu_3TaS_4	Solid-state Method [21,26]	800 °C for 48 h	-	light brown	-
	Cascade	TaS_2 , 300 °C for 2 h Cu_3TaS_4 , 300 °C for 1h	Cubic, ~20 nm	mustard-green	$1.38 \times 10^{-9} \text{ S}\cdot\text{m}^{-1}$
	Hot injection	300 °C for 1 h	Cubic, ~15 nm	yellow	
Cu_3TaSe_4	Solid-state Method [20]	Polycrystalline Powder 880 for 98 h Single crystals 890 for 143 h	Cubic	Orange yellow	-
	Cascade	TaSe_2 , 305 °C for 1 h Cu_3TaSe_4 , 305 °C for 1h	Cubic, irregular sizes	brown	weak resistance
	Hot injection	300 °C for 1 h	Core-shell, ~25 nm	brown	-

4. Conclusions

We demonstrated and evaluated the methodology dependence of nanostructural geometries in the tantalum sylvanites. Using a cascade synthesis method, cubic green-yellow Cu_3TaS_4 NCs and brown Cu_3TaSe_4 NCs were successfully prepared. The hot-injection method leads to green Cu_3TaS_4 NCs and brown Cu_3TaSe_4 NC with core-shell nanostructure. XRD patterns analysis of the products prepared with different reaction times showed that Cu_3TaS_4 NCs could be formed in very short time (1 min) after the addition of Cu cations when using the cascade method, whereas the hot-injection method requires 30 min to form Cu_3TaS_4 NCs. During the formation of Cu_3TaSe_4 using the cascade method, the incorporation of Cu cations triggered rapid nucleation of $\text{Cu}_{7.16}\text{Se}_4$ and then the formed $\text{Cu}_{7.16}\text{Se}_4$ consumed the folded TaSe_2 nanosheets to form Cu_3TaSe_4 NCs. While using the hot-injection method, the Cu_3TaSe_4 core-shells originated from $\text{Cu}_{7.16}\text{Se}_4$ seeds which rapidly formed within 1 min after adding the Cu-Ta precursors. The UV-Vis-NIR and photoluminescence measurements of the obtained Cu_3TaS_4 presented three characteristic absorbance peaks in the UV-Visible regions and unique emission peaks at 486.3 and 526.1 nm. The green emission of Cu_3TaS_4 at 526.1 nm suggests the presence

of a mid-band-gap charge trap caused by Cu vacancies near the valence band maximum. The absorption spectrum of Cu_3TaSe_4 NCs prepared by the cascade method shows three primary peaks at around 282.6, 339.6, and 393.5 nm. Surprisingly, the Cu_3TaSe_4 core-shells synthesized by the hot-injection method exhibit not only three primary peaks in the UV-Visible regions but also a unique absorption band at around 800–1000 nm; the phenomenon is currently investigated. Photoluminescence measurements of Cu_3TaSe_4 prepared by either cascade method or hot-injection shows an optical bandgap of 2.32 eV. In addition, the I-V curve of Au/ Cu_3TaSe_4 NCs-glass/Au device suggests the Cu_3TaSe_4 NCs possess nonnegligible conductivity properties. The preliminary optoelectronic study show potential of Cu_3TaSe_4 NCs as future transparent p-type conductors. Furthermore, the solution-based synthetic approaches of Cu_3TaSe_4 NCs and Cu_3TaSe_4 NCs provide grounds for future applications of these promising semiconductors in the p-type TCM realm.

Supplementary Materials: The following are available online at <https://www.mdpi.com/2073-4352/11/1/51/s1>, Figure S1: XRD of Cu_3TaSe_4 synthesized using stoichiometric ratio. Figure S2: Color changes for the cascade synthesis and hot-injection synthesis of Cu_3TaSe_4 NCs, Figure S3: XRD of Cu_3TaSe_4 synthesized using stoichiometric ratio, Figure S4: Color changes for the cascade synthesis and hot-injection synthesis of Cu_3TaSe_4 NCs, Figure S5: I-V curve of the Au/ Cu_3TaSe_4 NCs-glass/Au device.

Author Contributions: Formal analysis, M.L. and D.R.R.; data curation, M.L., C.-Y.C., C.-Y.L., and D.R.R.; writing—original draft preparation, M.L., C.-Y.L., and D.R.R.; writing—review and editing, D.R.R. and C.-Y.L.; supervision, D.R.R. and C.-Y.L.; project administration, D.R.R.; funding acquisition, D.R.R. and C.-Y.L. All authors have read and agreed to the published version of the manuscript.

Funding: 80NSSC19M0201. ML was funded by NASA, award number 80NSSC19M0201.

Institutional Review Board Statement: Not applicable.

Informed Consent Statement: Not applicable.

Acknowledgments: The authors are very grateful to Zhiqun Lin and his group at Georgia Institute of Technology for access to PL instrumentation.

Conflicts of Interest: The authors declare no conflict of interest.

References

1. Ginley, D.S.; Bright, C. Transparent Conducting Oxides. *MRS Bull.* **2000**, *25*, 15–18. [[CrossRef](#)]
2. King, P.D.C.; Veal, T.D. Conductivity in transparent oxide semiconductors. *J. Phys. Condens. Matter* **2011**, *23*, 334214. [[CrossRef](#)]
3. Granqvist, C.G. Transparent conductors as solar energy materials: A panoramic review. *Sol. Energy Mater. Sol. Cells* **2007**, *91*, 1529–1598. [[CrossRef](#)]
4. Calnan, S.; Tiwari, A.N. High mobility transparent conducting oxides for thin film solar cells. *Thin Solid Film.* **2010**, *518*, 1839–1849. [[CrossRef](#)]
5. Espinosa-García, W.F.; Pérez-Walton, S.; Osorio-Guillén, J.M.; Moyses Araujo, C. The electronic and optical properties of the sulvanite compounds: A many-body perturbation and time-dependent density functional theory study. *J. Phys. Condens. Matter* **2017**, *30*, 035502. [[CrossRef](#)] [[PubMed](#)]
6. Gordon, R.G. Criteria for Choosing Transparent Conductors. *MRS Bull.* **2000**, *25*, 52–57. [[CrossRef](#)]
7. Minami, T. Transparent conducting oxide semiconductors for transparent electrodes. *Semicond. Sci. Technol.* **2005**, *20*, S35–S44. [[CrossRef](#)]
8. Hosono, H. Recent progress in transparent oxide semiconductors: Materials and device application. *Thin Solid Film.* **2007**, *515*, 6000–6014. [[CrossRef](#)]
9. Ellmer, K. Past achievements and future challenges in the development of optically transparent electrodes. *Nat. Photonics* **2012**, *6*, 809–817. [[CrossRef](#)]
10. Angela, N.F.; Monica, M.-M. Bridging the p-type transparent conductive materials gap: Synthesis approaches for disperse valence band materials. *J. Photonics Energy* **2020**, *10*, 1–17.
11. Kawazoe, H.; Yanagi, H.; Ueda, K.; Hosono, H. Transparent p-Type Conducting Oxides: Design and Fabrication of p-n Heterojunctions. *MRS Bull.* **2000**, *25*, 28–36. [[CrossRef](#)]
12. Park, C.H.; Zhang, S.B.; Wei, S.-H. Origin of p-type doping difficulty in ZnO: The impurity perspective. *Phys. Rev. B* **2002**, *66*, 073202. [[CrossRef](#)]

13. Hosono, H.; Ueda, K. Transparent Conductive Oxides. In *Springer Handbook of Electronic and Photonic Materials*; Kasap, S., Capper, P., Eds.; Springer International Publishing: Cham, Switzerland, 2017; p. 1.
14. Kawazoe, H.; Yasukawa, M.; Hyodo, H.; Kurita, M.; Yanagi, H.; Hosono, H. P-type electrical conduction in transparent thin films of CuAlO₂. *Nature* **1997**, *389*, 939–942. [[CrossRef](#)]
15. Nagarajan, R.; Draeseke, A.D.; Sleight, A.W.; Tate, J. p-type conductivity in CuCr_{1-x}Mg_xO₂ films and powders. *J. Appl. Phys.* **2001**, *89*, 8022–8025. [[CrossRef](#)]
16. Farrell, L.; Norton, E.; Smith, C.M.; Caffrey, D.; Shvets, I.V.; Fleischer, K. Synthesis of nanocrystalline Cu deficient CuCrO₂—A high figure of merit p-type transparent semiconductor. *J. Mater. Chem. C* **2016**, *4*, 126–134. [[CrossRef](#)]
17. Dekkers, M.; Rijnders, G.; Blank, D.H.A. ZnIr₂O₄, a p-type transparent oxide semiconductor in the class of spinel zinc-d6-transition metal oxide. *Appl. Phys. Lett.* **2007**, *90*, 021903. [[CrossRef](#)]
18. Hiramatsu, H.; Ueda, K.; Ohta, H.; Orita, M.; Hirano, M.; Hosono, H. Heteroepitaxial growth of a wide-gap p-type semiconductor, LaCuOS. *Appl. Phys. Lett.* **2002**, *81*, 598–600. [[CrossRef](#)]
19. Ali, A.; Jahan, N.; Islam, A.K.M. Sulvanite Compounds Cu₃TMS₄ (TM= V, Nb and Ta): Elastic, Electronic, Optical and Thermal Properties using Firstprinciples Method. *J. Sci. Res.* **2014**, *6*, 407–419. [[CrossRef](#)]
20. Ali, S.; van Smaalen, S. Single crystal X-ray structure of Cu₃TaSe₄ and a comparative study of Cu₃MX₄ (M = V, Nb, Ta; X = S, Se, Te). *Z. Anorg. Allg. Chem.* **2014**, *640*, 931–934. [[CrossRef](#)]
21. Hersh, P.A. Wide Band Gap Semiconductors and Insulators: Synthesis, Processing and Characterization. Doctoral Dissertation, Oregon State University, Corvallis, OR, USA, 2007.
22. Ikeda, S.; Aono, N.; Iwase, A.; Kobayashi, H.; Kudo, A. Cu₃MS₄ (M=V, Nb, Ta) and its Solid Solutions with Sulvanite Structure for Photocatalytic and Photoelectrochemical H₂ Evolution under Visible-Light Irradiation. *ChemSusChem* **2019**, *12*, 1977–1983. [[CrossRef](#)]
23. Bougherara, K.; Litimein, F.; Khenata, R.; Uçgun, E.; Ocak, H.Y.; Uğur, Ş.; Uğur, G.Ö.K.A.Y.; Reshak, A.H.; Soyalp, F.; Omran, S.B. Structural, Elastic, Electronic and Optical Properties of Cu₃TMSe₄ (TM = V, Nb and Ta) Sulvanite Compounds via First-Principles Calculations. *Sci. Adv. Mater.* **2012**, *5*, 97–106. [[CrossRef](#)]
24. Li, Y.; Wu, M.; Zhang, T.; Qi, X.; Ming, G.; Wang, G.; Quan, X.; Yang, D. Natural sulvanite Cu₃MX₄ (M = Nb, Ta; X = S, Se): Promising visible-light photocatalysts for water splitting. *Comput. Mater. Sci.* **2019**, *165*, 137–143. [[CrossRef](#)]
25. Kehoe, A.B.; Scanlon, D.O.; Watson, G.W. The electronic structure of sulvanite structured semiconductors Cu₃MCh₄ (M = V, Nb, Ta; Ch = S, Se, Te): Prospects for optoelectronic applications. *J. Mater. Chem. C* **2015**, *3*, 12236–12244. [[CrossRef](#)]
26. Nitsche, R.; Wild, P. Crystal Growth and Electro-optic Effect of Copper-Tantalum-Selenide, Cu₃TaSe₄. *J. Appl. Phys.* **1967**, *38*, 5413–5414. [[CrossRef](#)]
27. Petritis, D.; Martinez, G.; Levy-Clement, C.; Gorochoy, O. Investigation of the vibronic properties of Cu₃VS₄, Cu₃NbS₄, and Cu₃TaS₄ compounds. *Phys. Rev. B* **1981**, *23*, 6773–6786. [[CrossRef](#)]
28. Newhouse, P.F.; Hersh, P.A.; Zakutayev, A.; Richard, A.; Platt, H.A.S.; Kesler, D.A.; Tate, J. Thin film preparation and characterization of wide band gap Cu₃TaQ₄ (Q = S or Se) p-type semiconductors. *Thin Solid Film.* **2009**, *517*, 2473–2476. [[CrossRef](#)]
29. Liu, M.; Lai, C.-Y.; Selopal, G.S.; Radu, D.R. Synthesis and optoelectronic properties of Cu₃VSe₄ nanocrystals. *PLoS ONE* **2020**, *15*, e0232184. [[CrossRef](#)]
30. Schmidt, K.H.; Müller, A.; Bouwma, J.; Jellinek, F. Übergangsmetall-chalklogen-verbindungen IR-und raman-spektren von Cu₃MX₄ (m = v, nb, ta; x = s, se). *J. Mol. Struct.* **1972**, *11*, 275–282. [[CrossRef](#)]
31. Liu, M.; Lai, C.-Y.; Zhang, M.; Radu, D.R. Cascade synthesis and optoelectronic applications of intermediate bandgap Cu₃VSe₄ nanosheets. *Sci. Rep.* **2020**, *10*, 21679. [[CrossRef](#)]
32. Sarkar, S.; Leach, A.D.P.; Macdonald, J.E. Folded Nanosheets: A New Mechanism for Nanodisk Formation. *Chem. Mater.* **2016**, *28*, 4324–4330. [[CrossRef](#)]
33. Barbir, F. Chapter Four-Main Cell Components, Material Properties, and Processes. In *PEM Fuel Cells*, 2nd ed.; Barbir, F., Ed.; Academic Press: Boston, MA, USA, 2013; pp. 73–117.
34. Sha, W.; Wu, X.; Keong, K.G. 8-Electrical resistivity of electroless copper deposit. In *Electroless Copper and Nickel-Phosphorus Plating*; Sha, W., Wu, X., Keong, K.G., Eds.; Woodhead Publishing: Cambridge, UK, 2011; pp. 117–134.
35. Hassanien, A.S.; Akl, A.A. Electrical transport properties and Mott’s parameters of chalcogenide cadmium sulphoselenide bulk glasses. *J. Non Cryst. Solids* **2016**, *432*, 471–479. [[CrossRef](#)]
36. Hassanien, A.S.; Akl, A.A. Effect of Se addition on optical and electrical properties of chalcogenide CdSSe thin films. *Superlattices Microstruct.* **2016**, *89*, 153–169. [[CrossRef](#)]
37. Santos, T.G. 5-Characterization of FSP by electrical conductivity. In *Surface Modification by Solid State Processing*; Miranda, R., Ed.; Woodhead Publishing: Cambridge, UK, 2014; pp. 153–176.
38. Singh, Y. Electrical Resistivity Measurements: A review. *Int. J. Mod. Phys. Conf. Ser.* **2013**, *22*, 745–756. [[CrossRef](#)]
39. Ehrstein, J.R. Two-Probe (Spreading Resistance) Measurements for Evaluation of Semiconductor Materials and Devices. In *Nondestructive Evaluation of Semiconductor Materials and Devices*; Zemel, J.N., Ed.; Springer: Boston, MA, USA, 1979; pp. 1–66.
40. Jeong, S.; Yoo, D.; Jang, J.-T.; Kim, M.; Cheon, J. Well-Defined Colloidal 2-D Layered Transition-Metal Chalcogenide Nanocrystals via Generalized Synthetic Protocols. *J. Am. Chem. Soc.* **2012**, *134*, 18233–18236. [[CrossRef](#)] [[PubMed](#)]

-
41. Grima-Gallardo, P.; Salas, M.; Contreras, O.; Power, C.; Quintero, M.; Cabrera, H.; Zumeta-Dubé, I.; Rodríguez, A.; Aitken, J.; Brämer-Escamilla, W. Cu_3TaSe_4 and Cu_3NbSe_4 : X-ray diffraction, differential thermal analysis, optical absorption and Raman scattering. *J. Alloy. Compd.* **2016**, *658*, 749–756. [[CrossRef](#)]
 42. Espinosa-García, W.F.; Valencia-Balvín, C.; Osorio-Guillén, J.M. Phononic and thermodynamic properties of the sulvanite compounds: A first-principles study. *Comput. Mater. Sci.* **2016**, *113*, 275–279. [[CrossRef](#)]